Radiation-accelerated Precipitation in Fe-Cr alloys

Frédéric Soisson and Thomas Jourdan

CEA, DEN, Service de Recherches de Métallurgie Physique, UPSay, F-91191 Gif-sur-Yvette, France

Abstract

The kinetics of phase separation in Fe-Cr alloys under irradiation is modeled by Atomistic kinetic Monte Carlo simulations that include the formation, migration and elimination of vacancies and self-interstitials at point defects sinks. The evolution of the sink density is modeled by cluster dynamics, and taken into account in the Monte Carlo simulations by a rescaling of the time. The results are in good agreement with available experimental observations of neutron irradiation at 290°C. The irradiation is found to accelerate the kinetics of phase separation by orders of magnitude, with an acceleration factor given by the increase in point defect concentrations. The microstructure evolution is qualitatively the same as during isothermal annealing, except in the vicinity of point defect sinks. The effects of equilibrium and radiation induced segregations at grain boundaries are considered. The ballistic mixing occurring in displacement cascades is modeled, and is found to be insufficient to produce the dissolution of chromium rich precipitates at 290°C, even at high dose rates. Therefore, it cannot explain the absence of precipitation observed during ion irradiations.

Keywords: Precipitation kinetics, Monte Carlo Simulations, Irradiation Effect, Fe-Cr alloy

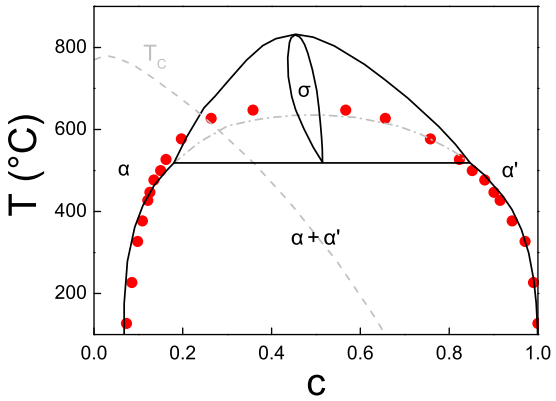

Figure 1: The Fe-Cr Phase Diagram, from Ref. [2] (the circles show the miscibility gap of the AKMC model).

1. Introduction

Iron-chromium alloys are the model system of ferritic and ferritic-martensitc steels that will be used in future fission (generation IV) and fusion nuclear reactors. Below approximately 600°C (Fig. 1), Fe-Cr solid solutions undergo a coherent phase separation between an iron rich phase (α) and a chromium rich phase (α'), with body centered cubic (bcc) lattices and very close lattice parameters. This decomposition is the origin of the "475°C Embrittlement", a phenomenon known since the thirties and that has been related to the α' precipitation in 1953 [1].

Kinetics of isothermal precipitation in Fe-Cr alloys have been extensively studied by small-angle neutron scattering (SANS) [3, 4], Mössbauer Spectroscopy [5–7], field ion microscopy and 3D atom probe (3DAP) [8–13]. Most of these studies deal with relatively highly concentrated alloys at temperatures of 450°C or above, where precipitation kinetics is rapid enough. At lower temperatures α' precipitation becomes slower, even in highly supersaturated alloys: for example, it is not observed in a Fe-32%Cr alloys after an isothermal annealing of

2150h at 290°C [14]. As usual, because of slow kinetics the low temperature region of the phase diagram is mainly known from extrapolation from higher temperatures, leading to some controversies [2, 15]. But for nuclear applications with Cr concentrations between 8 and 12% [16], or even 14% for the matrix of some oxide dispersion-strengthened steels [17], one may expect a α' precipitation: according to the most recent phase diagrams (Fig. 1), at $T < 300$°C for 9% of Cr, at $T < 450$°C for 14% of Cr. The precipitation may be too slow to be observed during isothermal annealing on accessible times, but it can be strongly accelerated by irradiation, because point defect concentrations may then be higher than the equilibrium ones (by orders of magnitude), leading to much faster diffusion. Indeed, α' precipitation has been observed under neutron irradiations: at 290°C in model alloys with 9 to 18% of Cr [18] and with 32% of Cr [14], at 300°C in Fe-12%Cr [19, 20] and Fe-12.5%Cr [21] alloys, at 325°C in martensitic steels with 7 and 11% of Cr [22], at 300 and 450°C in 10 and 16%Cr models alloys [23]. On the opposite, a recent study [24] has shown no α' precipitates in a Fe-12%Cr alloy irradiated by ions at 300°C, while they were observed in the same alloy during neutron irradiation at the same temperature, with a lower dose rate (7×10^{-7} instead of 2×10^{-4}dpa.s^{-1}). On the modeling side, cluster dynamics has been used to model the acceleration of Cr precipitation in Fe-12.5%Cr at 300°C: the experimental kinetics were successfully reproduced by using the α/α' interface energy as a fitting parameter [25].

Besides a strong acceleration, these experiments show few differences in the precipitate microstructure between isothermal agings and irradiations. One exception is the study of a Fe-32%Cr alloy irradiated by neutrons at 290°C: isolated α' precipitates were observed [14], while alloys with such high Cr contents usually display bi-percolated microstructures when annealed without irradiation at higher temperatures. Moreover, the Cr solubility limit was found to be much

higher under irradiation than at equilibrium ($\simeq 30\%$, instead of $\simeq 9\%$). Both effects were attributed to the ballistic mixing occurring within displacement cascades [14]. These conclusions seem hardly compatible with the experiments of Mathon et al. [22], performed at a slightly higher temperature (325°C), suggesting a much lower solubility, close to the equilibrium one. Another difference with isothermal annealing is the observation under irradiation of precipitate free zones (PFZ) in the vicinity of cavities [26], grain boundaries, or other incoherent precipitates (such as carbides or nitrides [27]). To our knowledge, this has not been observed for α' precipitation without irradiation.

The aim of the present study is to model the kinetics of $\alpha - \alpha'$ phase separation under irradiation and especially to quantify the acceleration due to the point defect supersaturation. We also consider possible effects that could qualitatively change the precipitation microstructure, such as those of ballistic mixing and of grain boundaries. We use Atomistic Kinetic Monte Carlo (AKMC) simulations that take into account the diffusion of Fe and Cr by vacancy and self-interstitials, including the formation, migration, mutual recombination and annihilation of these point defects at sinks. The parameters of the model have been fitted to ab initio calculations and it has been successfully applied to model kinetics of precipitation during isothermal annealing [28, 29] and radiation induced segregation [30].

A key point to model the acceleration of precipitation is to deal with realistic point defects concentrations. Therefore in section 2, we first recall some important aspects of radiation effects on point defect concentrations and diffusion, as revealed by homogeneous kinetic equations and cluster dynamics, emphasizing especially the role of dose rate and point defect sink densities. In section 3 we present the AKMC simulations that are performed using different dose rates and different, but constant, sink densities. We explain how they can be improved

to take into account a more detailed evolution of the sink densities, as given by cluster dynamics. The results of the simulations are presented in section 4 and compared with experimental results.

2. Point defect concentrations and diffusion under irradiation

The diffusion coefficients of substitutional elements (in our case, Fe and Cr) are proportional to point defect concentrations. In a pure metal for example, if the contribution of di-vacancies, di-interstitials and other point defect clusters are negligible, the self-diffusion coefficient is given by:

$$D^* = f_i c_i D_i + f_v c_v D_v \tag{1}$$

where D_i and D_v are the diffusion coefficients of vacancies and self-interstitials, f_i and f_v some correlation factors (in pure metals, constants close to 1), c_i and c_v the point defect concentrations [31, 32]. Under irradiation these concentrations may be much higher than the equilibrium values, c_i^{eq} and c_v^{eq}. Several rate theory models have been proposed to estimate the evolution of c_i and c_v. Most simple ones only consider mono-vacancies and mono-interstitials in a homogeneous system, with concentration evolutions given by:

$$\begin{aligned} \frac{dc_v}{dt} &= G - Rc_i c_v - \sum_s k_{sv}^2 D_v (c_v - c_{sv}) = G - Rc_i c_v - K_v (c_v - c_v^{eq}) \\ \frac{dc_i}{dt} &= G - Rc_i c_v - \sum_s k_{si}^2 D_i (c_i - c_{si}) = G - Rc_i c_v - K_i (c_i - c_i^{eq}) \end{aligned} \tag{2}$$

G is the point defect production rate, or dose rate (in dpa.s^{-1}), $R = 4\pi r_c (D_i + D_v)/\Omega$ is the rate of recombination between vacancies and interstitials (where Ω is the atomic volume and r_c the distance of spontaneous recombination). The third terms in Eq. (2) correspond the elimination of point defects on the different sinks s of the microstructures: grain boundaries, free surfaces, point

defect clusters, etc. c_{sv} and c_{si} are the point defects concentrations at the sinks (where they remain at their equilibrium values, $c_{sv} = c_v^{eq}$ and $c_{si} = c_i^{eq}$). The sink strengths k_{sv}^2 and k_{si}^2 have been computed for common sinks [33]. For example, for a thin film geometry with planar sinks separated by a distance L, $k_s^2 \simeq 12/L^2$.

Usually $c_v \gg c_v^{eq}$ and $c_i \gg c_i^{eq}$, and the steady-state solutions of Eq. (2) are:

$$\begin{aligned} c_v^{st} &= -\frac{K_i}{2R} + \sqrt{\frac{K_i^2}{4R^2} + \frac{GK_i}{RK_v}} \\ c_i^{st} &= -\frac{K_v}{2R} + \sqrt{\frac{K_v^2}{4R^2} + \frac{GK_v}{RK_i}} \end{aligned} \tag{3}$$

Time evolutions are easily obtained by numerical integration of Eq. (2). Using Eq. (1), and considering that Eq. (2) imposes $c_i D_i \sim c_v D_v$ in the steady-state, diffusion under irradiation is accelerated by a ratio $2(c_v^{st}/c_v^{eq})$ after a short transient regime.

In simple cases the sink microstructure and the sink strength are supposed to be constant, but in general they evolve during the irradiation, although much more slowly than the point defect concentrations. The annihilation of point defects on pre-existing dislocations can produce a climb of the dislocation network, and point defects can form vacancy or interstitial clusters directly in displacements cascades or after subsequent evolution. Cluster dynamics (CD) methods, based on generalized rate theory equations, give the evolution of clusters of j defects, according to :

$$\frac{dc_j}{dt} = G_j + \sum_k w(k,j)c_j - \sum_k w(j,k)c_j - L_j \tag{4}$$

where G_j is the production rate of clusters of j defects, $w(k,j)$ and $w(j,k)$ the rate of absorption or emission of a cluster of size j by a cluster of size k, and L_j gives the rate of elimination of the clusters on the sinks other than

point defects clusters. In the following, we will use the CD code Crescendo [34], with the parameters determined by Meslin et al. [35] to fit electron microscopy observations of clusters formed during ion irradiation of iron.

3. Monte Carlo Simulations

Atomistic Kinetic Monte Carlo (AKMC) methods allow a simulation of the $\alpha - \alpha'$ decomposition, directly based on realistic diffusion mechanisms. We use here the AKMC code and parameters developed by Senninger et al. [30] to study radiation-induced segregation (RIS) in Fe-Cr alloys (simpler versions have been previously applied to the study of $\alpha - \alpha'$ phase separation during isothermal annealing [28, 29]).

The model takes into account the diffusion of mono-vacancies and self-interstitials with $\langle 110 \rangle$ dumbbell configurations (the most stable one in Fe-Cr alloys). Migration barriers are computed with a broken-bond model and effective pair interactions fitted to ab initio calculations. The pair interactions depend on the temperature and the local composition, to take into account vibrational and magnetic contributions, especially important in these alloys [28–30]. In this way, the asymmetrical $\alpha - \alpha'$ miscibility gap (Fig. 1) and the experimental diffusion properties of Fe-Cr alloys in a large domain of temperatures and compositions, are well reproduced [29]. The modeling of point defect concentrations, and their evolutions, depend on the situation.

3.1. Thermal aging

During isothermal annealing (no irradiation), only vacancy diffusion is relevant and one may assume that vacancy concentrations remain at equilibrium during the phase separation. Only one vacancy is introduced in the AKMC simulation, but the time is rescaled to take into account the real vacancy concentration and its change during the evolution of the precipitate microstructure

[28, 36]. Simulations are performed in cubic systems with $N = 2 \times 64^3$ or $N = 2 \times 128^3$ lattice sites and periodic boundary conditions (the small size is used to simulate long annealing times, the largest one to get better statistics).

3.2. Irradiation

Point defect concentrations are no more at equilibrium, and their formation and elimination mechanisms are introduced in the simulations [37]. Several formation mechanisms of point defects are used, in order to assess the effect of ballistic mixing on the precipitation kinetics (in the following we use the common terminology: displacements refers to the formation of point defects, replacements to atoms that change of site but remain on the bcc lattice):

- Channeling mechanism (CHA): one vacancy is created on a randomly chosen lattice site, and the atom initially located on this site forms a dumbbell with another atom, located at a distance of 10 nearest neighbor (nn) in one of the eight $\langle 111 \rangle$ dense directions, randomly chosen. No replacement occurs between the vacancy and interstitial sites.

- Replacements collisions sequences (RCS): one vacancy is created on a randomly chosen lattice site and a series of 10 replacements is produced in one of the eight $\langle 111 \rangle$ dense directions, randomly chosen. The two atoms at the end of the sequence form a dumbbell. 10 replacements are therefore produced for each displacement.

- Replacement cascades (CAS): one vacancy is created on a randomly chosen lattice site, the atom initially located on this site forms a dumbbell with an atom randomly chosen within a sphere with a radius of 10 nn around the initial atom. A series of 100 replacements is performed between pairs of atoms randomly chosen within the same sphere.

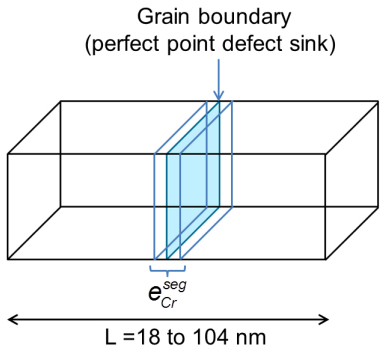

Figure 2: Point defect sinks geometry of the AKMC simulations

The first two mechanisms are typical of electron irradiations, the third one takes into account some key features of ion or neutron irradiation: the large number of replacements in displacements cascades that produce a local chemical disorder. On the other hand it does not reproduce the direct formation of small interstitial and vacancy clusters, typical of these irradiation conditions. In each case, the frequency associated with the Frenkel pair formation is given by the dose rate (in dpa.s^{-1}).

Point defects disappear by:

- Mutual recombination, when the distance between a vacancy and an interstitial is below a given recombination radius r_c (4 nn distances).
- Annihilation on sinks. We have chosen a simple sink geometry (Fig. 2): the system contains a simple model of grain boundary (GB), constituted of a plane of lattice sites, acting as perfect sinks. With periodic boundary conditions, it corresponds to a microstructure of parallel grains, with distances L between the GBs. Equilibrium segregation at GBs is accounted for by adding extra energetic terms e_{Cr}^{seg} when Cr atoms are located on the sites of the GB, and of two neighboring planes (see 4.4 for details).

The simulations are performed in cubic simulations boxes with $N = 2 \times 64^3$ or $N = 2 \times 128^3$ bcc lattice sites and a GB along a {100} plane (with $L = 64a \sim 18\,\text{nm}$ or $128a \sim 37\,\text{nm}$) or in rhombohedral boxes with $N = 64 \times 64 \times 512$ bcc sites and a GB along a {110} plane (with $L = 256\sqrt{2}a \sim 104\,\text{nm}$).

The different events are chosen with a residence time algorithm [30, 37]. Since formation and annihilation mechanisms are directly reproduced, one gets point defect concentration and a time t_{MC} representative of the chosen irradiation conditions: temperature, dose rate and the sink density in the simulation box.

3.3. Evolution of sink density and time rescaling by cluster dynamics

The previous geometry makes it easy to control the sink strength and to measure Cr and point defect concentration profiles around grain boundaries. An important limitation is that the sink density and strength are imposed and constant ($k_s^2 \simeq 12/L^2$). According to Eq. (2)-(3), point defect concentrations are therefore not the same in the AKMC simulations and in the experiments: their time scales and precipitation kinetics are not directly comparable. Indeed, a distance of 18 or even 104 nm between GBs corresponds to a very small grain size, and the corresponding sink strength is too high. On the opposite, other point defect sinks, especially point defect clusters, are not included in the simulations.

We have therefore used the CD model to get more reliable estimation of the total sink strengths and point defect concentrations. We use the parameters of Ref. [35] which are, strictly speaking, only valid for pure iron. An addition of 10 to 20% of Cr must modify the point defect diffusion coefficients [30] and the stability and migration of point defect clusters. However, if this can strongly affect the distribution of point defect clusters, the total dislocation density and the total sink strength are probably less sensitive to such details, being mainly

determined by the number of vacancies and interstitials (at least in conditions where recombinations are negligible).

An example of CD calculation is shown in Fig. 3(a). It gives the evolution of the total sink strength, together with the contributions of the different kinds of sinks, for a neutron irradiation in conditions closed to the study of Bachhav et al. [18] (290°C, 3.4×10^{-7}dpa.s^{-1}, dislocation density $\rho_d = 10^8$cm^{-2}, grain size $200\,\mu$m). The results correspond to high density sinks at 290°C the elimination of point defects by mutual recombination is negligible, Eq. (3) gives $c_v^{st} \simeq G/K_v$ and $c_i^{st} \simeq G/K_i$.

At the beginning of the irradiation, the dominant sinks are the dislocations of the initial dislocation network. Very rapidly the vacancy clusters formed in displacement cascades prevail. The contribution of interstitial clusters always remains one or two orders of magnitude lower and the one of grain boundaries is negligible.

Figure 3(b) compares the total sink strength of the cluster dynamics with the constant one of the AKMC simulations, for different distances between sinks. Because of the very high density of grain boundaries, the sink strength is initially overestimated in the AKMC simulations. On the opposite for high irradiation doses (~ 1 dpa), the sink strength is underestimated in AKMC simulations (especially for large L). The physical time scale corresponding to the experimental conditions can be obtained by rescaling the Monte Carlo time according to:

$$t = t_{MC} \times \frac{c_d(AKMC)}{c_d(CD)} \tag{5}$$

When elimination by recombination is negligible: $c_{i,v}^{st} \simeq G/(k_s^2 D_{i,v})$ and $t = t_{MC} \times k_d^2(CD)/k_d^2(AKMC)$. In practice, AKMC simulations are performed with the time scale corresponding to a constant sink strength, CD calculations are performed for a set of parameters (temperature, dose rate, dislocation density,

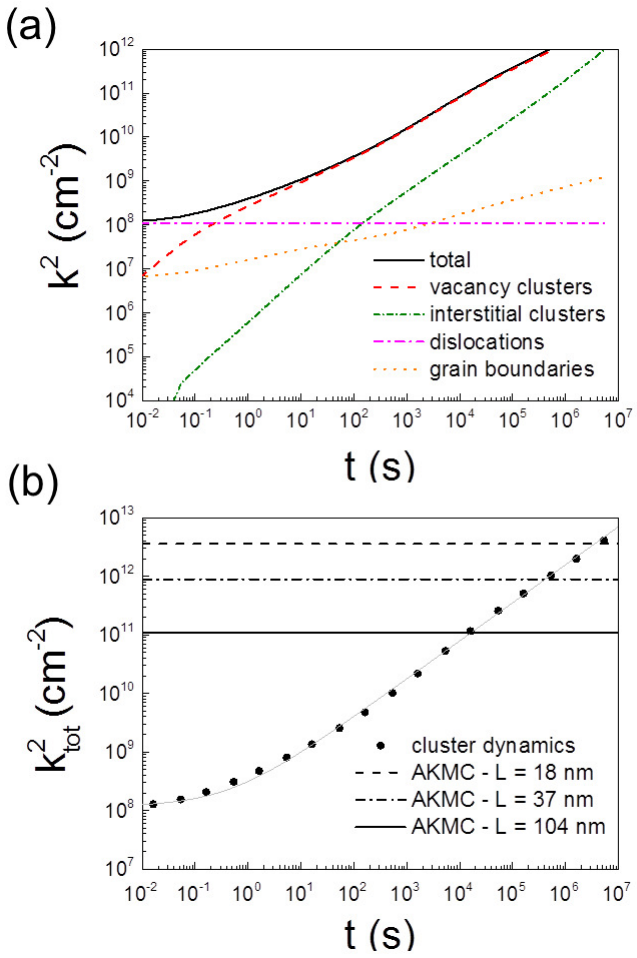

Figure 3: Evolution of the sink strengths in α-Fe under neutron irradiation at 290°C and 3.4×10^{-7}dpa.s^{-1}, computed by cluster dynamics. (a) Contribution of the different sinks (b) Evolution of the total sink strength, compared with the constant sink strength in AKMC simulations (estimated to $k^2_{tot} = 12/L^2$, for different distances L between the grain boundaries).

grain size) corresponding to the experimental conditions and the AKMC time is rescaled by Eq. (5).

4. Kinetics of decomposition under irradiation

4.1. Acceleration of the phase separation

Bachhav et al. [18] have observed by 3DAP the α' precipitation in Fe-Cr alloys with Cr contents between 3 and 18% of Cr, during neutron irradiations at 290°C, with a dose rate of 3.4×10^{-7}dpa.s^{-1} and up to a fluence of 1.82 dpa. For 9, 12, 15 and 18% of Cr, they observed a homogeneous α' precipitation, with a precipitate density increasing rapidly with the Cr concentration. No precipitation was observed in Fe-3%Cr and Fe-6%Cr alloys. We have performed AKMC simulations with the same temperature and compositions, under irradiation at the same dose rate, as well as during isothermal annealing at the same temperature. Simulations under irradiation have been firstly performed with the channeling formation mechanism of Frenkel pairs, two distances (L = 37 and 104 nm) between point defects sinks, and no equilibrium segregation tendency at GBs ($e_{Cr}^{seg} = 0$).

4.1.1. Precipitation in Fe-15%Cr

Let us first consider the α' precipitation in the Fe-15%Cr alloy. Typical precipitate microstructures are shown in Fig. 4 (isothermal annealing) and 5 (irradiation). In both cases one observes a nucleation and growth of isolated α' precipitates, the main differences being that under irradiation a precipitate free zone of a few nanometers surrounds the GB, and that the kinetics is much more rapid.

Point defect concentrations. To analyze the acceleration, it is important to consider the point defect concentration profiles under irradiation, and the effect of

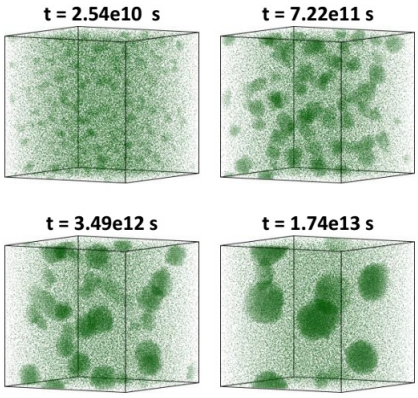

Figure 4: AKMC simulations of $\alpha - \alpha'$ phase separation in Fe-15%Cr during an isothermal annealing at 290°C (with $N = 2 \times 64^3$ bcc sites, only the Cr atoms are shown).

the Cr concentration and the sink density. Fig. 6 gives the point defect concentration profiles measured in AKMC simulations in Fe-15%Cr and, for comparison, in pure iron. They are measured at the end of simulations, but indeed the point defect concentrations stabilizes very rapidly, in practice as soon as they can be measured [37]. In pure iron the steady-state concentrations (far from the GB) are $c_v^{st} \simeq 10^{-11}$ and $c_i^{st} \simeq 1.6 \times 10^{-14}$ for $L = 37\,\text{nm}$, close to the values predicted by Eq. (3): $c_v^{st} \simeq 8.5 \times 10^{-12}$ and $c_i^{st} \simeq 1.3 \times 10^{-14}$ [Fig. 6(a)]. For the larger $L = 104\,\text{nm}$, the AKMC simulations give: $c_v^{st} \simeq 4.8 \times 10^{-11}$, $c_i^{st} \simeq 7.5 \times 10^{-14}$ and Eq. (3): $c_v^{st} \simeq 6.8 \times 10^{-11}$, $c_i^{st} \simeq 1.1 \times 10^{-13}$ [Fig. 6(b)]. These concentrations are well above the equilibrium value: $c_v^{eq} \simeq 2.2 \times 10^{-18}$ at 290°C (with a vacancy formation energy $E_v^{for} = 2.17\,\text{eV}$ and a formation entropy $S_v^{for} = 4.1 k_B$ in pure iron [29]). As expected, they increase when L increases. The approximate values $c_v^{st} \simeq G/K_v$ and $c_i^{st} \simeq G/K_i$ (for high densities of sinks) give the same results as Eq. (3).[1]

[1] AKMC values are close to the predictions of Eq. (3), but they are indeed slightly higher for $L = 37\,\text{nm}$, and slightly smaller for $L = 104\,\text{nm}$. Eq. (3) predicts that c_v^{st} and c_i^{st} are proportional to L^2, so that they should increase by a factor 8 between $L = 37$ and 104 nm. AKMC rather gives a factor 5. This discrepancy is due to the shape of the system used in the AKMC simulations with $L = 104\,\text{nm}$ (a box of $N = 64 \times 64 \times 512$ bcc lattice sites elongated

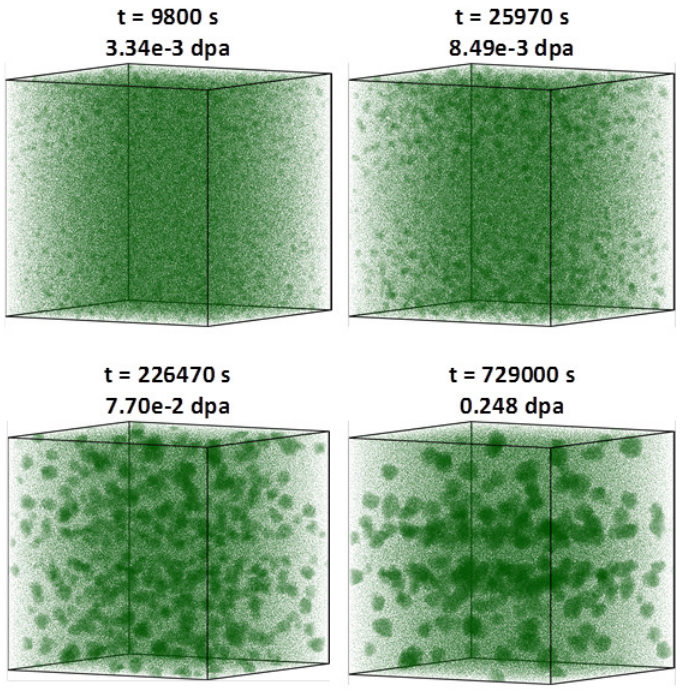

Figure 5: AKMC simulations of $\alpha - \alpha'$ phase separation in Fe-15%Cr under an irradiation at 290°C and 3.4×10^{-7}dpa.s^{-1} (with $N = 2 \times 128^3$ bcc sites and a distance $L = 37$ nm between GBs, the GB is located in the middle of the vertical direction)

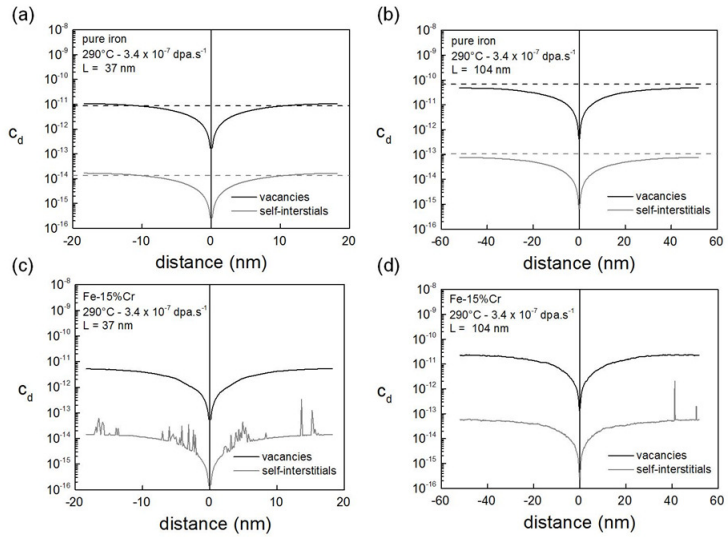

Figure 6: Steady-state point defect concentration profiles in the vicinity of a grain boundary, measured in AKMC simulations, in pure Fe and in Fe-15%Cr, under irradiation at 290°C and 3.4×10^{-7}dpa.s^{-1}, for two distances between the GBs ($L = 37$ and 104 nm). The dashed lines gives the steady-state concentrations predicted by Eq. (2), in pure iron.

By comparison with pure iron, the steady-state concentrations in the Fe-15%Cr alloy [see Fig. 6(c) and (d)] mostly exhibit a decrease by a factor 2 for the vacancies: $c_v^{st} \simeq 5 \times 10^{-12}$ and $c_v^{st} \simeq 2.3 \times 10^{-11}$ respectively for $L = 37$ and 104 nm (the self-interstitial concentrations are almost the same as in pure iron). This is due to the fact that at 290°C, an addition of 10 to 15% of Cr increases the diffusion coefficient of vacancies by the same factor, and has no significant effect of the interstitial diffusion coefficient [30]. In the Fe-15%Cr alloy as in pure iron, point defect concentrations will be therefore ~ 5 times larger with $L = 104$ nm than with $L = 37$ nm.

---

in the ⟨110⟩ direction). With such shape and periodic boundary, vacancy and interstitial diffusing along lateral directions recombine more frequently before reaching the GB than in a system of $512 \times 512 \times 512$ lattice site: the number of recombinations is then artificially increased. We have checked that simulations with $N = 2 \times 128^3$ and $N = 512 \times 512 \times 512$ differ by a factor 8 in steady-state point defect concentrations, but unfortunately they are too time consuming to study the precipitation kinetics.

Microstructure evolution. Fig. 7 gives the evolutions of the density d_p and the average radius R_p of α' precipitates,[2] corresponding to the microstructure evolutions of Fig. 4 and 5. The experimental values of Ref. [18] (only available at 1.82 dpa) are shown for comparison. The full lines show the results of AKMC simulations with the time scale corresponding to the constant sink strength, i.e. with the point defect concentrations discussed in the previous paragraph. The dashed lines give the kinetics after rescaling by Eq. (5), taking into account the evolution of the sink strength computed by CD.

During isothermal annealing as well as under irradiation, the evolutions of d_p and R_p correspond qualitatively to classical nucleation, growth and coarsening regimes. During isothermal annealing, the precipitation is very slow: the maximum density of precipitates ($d_p^{max} \simeq 3 \times 10^{19}\text{cm}^{-3}$, with $R_p \simeq 0.67\,\text{nm}$) is reached after 4×10^{10}s (approximately 1300 years). Under irradiation at $3.4 \times 10^{-7}\text{dpa.s}^{-1}$ and using first the non-rescaled time (full lines in Fig. 7), it is reached after only 2.9×10^4s with $L = 37\,\text{nm}$, and 5.4×10^3s with $L = 104\,\text{nm}$, i.e. with acceleration factors between 6 and 7 orders of magnitude. The acceleration is due to the point defect supersaturation: the difference between the kinetics with $L = 37$ and $L = 104\,\text{nm}$ corresponds to the factor 5 between the point defect concentrations [Fig. 6(c) and (d)], and by comparison with the equilibrium concentration of vacancies $c_v^{eq} \simeq 2 \times 10^{-18}$, one gets $2(c_v^{st}/c_v^{eq}) \simeq 5 \times 10^6$ and 2×10^7 depending on L. For a given distance L, we have also observed the same evolutions of d_p and R_p, and similar microstructures, with GBs along {100} and {110} planes.

[2] Clusters of 50 or more Cr atoms are considered as α' precipitates. The radius of a precipitate is given by $R_p = [(3n_{Cr}\Omega)/(4\pi)]^{1/3}$, where n_{Cr} is the number of Cr atoms in the cluster. We assume a spherical shape and we use the same definition as in Ref. [18], for a direct comparison with the experiments. The Fe atoms within the α' precipitates ($\sim 15\%$ at 290°C), are neglected, which (as noted in [18]) can lead to a underestimation of the precipitate radius of the order of 0.1 nm.

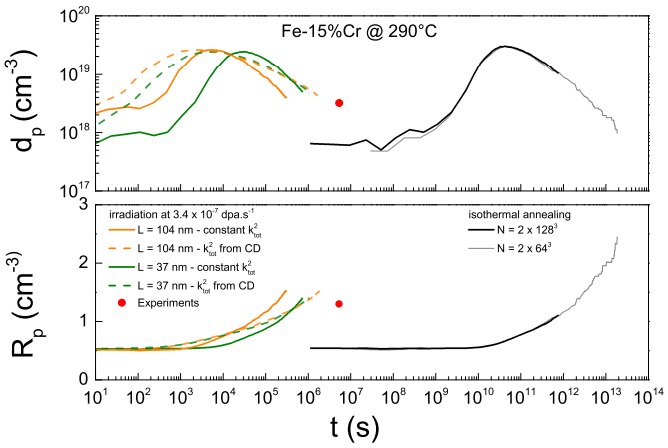

Figure 7: AKMC simulations of $\alpha - \alpha'$ phase separation in Fe-15%Cr during an isothermal aging at 290°C and under irradiation at 3.4×10^{-7}dpa.s^{-1}: evolution of the density d_p and of the average radius R_p of α' precipitates.

Except for this strong acceleration, the evolutions of d_p and R_p appear qualitatively similar under irradiation and during isothermal annealing, they are simply shifted towards shorter times. This is in agreement with the similarity of microstructures in Fig. 4 and 5, which only differ in the vicinity of the GB. The PFZ formed in this region under irradiation is due to the low point defect concentrations near the sink (Fig. 6) that lead to a slower diffusion of Cr, and prevent the nucleation and growth of precipitates. It explains that the maximum density of precipitates is slightly smaller under irradiation ($d_p^{max} \simeq 2.4 \times 10^{19}$cm^{-3} for $L = 37$ nm, $d_p^{max} \simeq 2.6 \times 10^{19}$cm^{-3} for $L = 104$ nm). The precipitates that nucleate and grow on both sides of the PFZ can absorb the corresponding excess of Cr atoms, leading to the formation of a layer with a locally higher density of precipitates (Fig. 5). When the distance L between sinks increases, the relative importance of the precipitate free zone decreases and d_p^{max} approaches the value of the isothermal annealing (3×10^{19}cm^{-3}).

The kinetics predicted by the simulations without correction of the time scale are too fast by approximately one order of magnitude at large doses. Fig. 3(b)

shows that it is due to the underestimation of the sink strength. At small times, CD predicts a much lower sink strength than AKMC simulations, therefore higher point defect concentrations: the AKMC simulations underestimate the acceleration. On the contrary, at longer times ($t > 2 \times 10^3$s for $L = 104$ nm, $t > 5 \times 10^5$s for $L = 37$ nm), CD predicts a higher sink strength and lower point defect concentrations than AKMC, due to the formation of a high density of small vacancy clusters.

When the time is rescaled according to Eq. (5) that take into account the evolution of the sink strength predicted by CD (dashed lines in Fig. 7), the AKMC kinetics are in better agreement with the experiments (although simulations predict a radius slightly larger than the experimental one). The comparison suggests than the precipitation microstructures observed at 1.82 dpa in the experiments [18] are already in the coarsening stage. Note that since the time rescaling corrects the effect of sink densities, the kinetics becomes almost independent of L: one gets the same evolution for the precipitate radius. There is a small difference between the densities obtained with $L = 37$ and 104 nm, for times below 1000 s, due to the PFZ.

4.2. Effect of the Cr content

In Fe-9%Cr alloys, the Cr concentration is too close to the solubility limit to observe a precipitation in the AKMC simulations (a detailed analysis of SANS experiments gives a solubility of $8.5 \pm 0.2\%$ at 300°C [21], in the present model is it slightly larger: $9 \pm 0.1\%$ at 290°C). Simulations performed with 12 and 18% are summarized in Fig. 8 to 10. The acceleration under irradiation is approximately the same as in the Fe-15%Cr alloy, i.e. 6 or 7 orders of magnitude. The maximum density of precipitates strongly increases with the supersaturation: $d_p^{max} \simeq 2 \times 10^{18}$, 3×10^{19}, and 6×10^{19}cm^{-3} for respectively 12, 15, and 18%Cr; and during thermal aging it is reached after more than 5×10^{11}s in

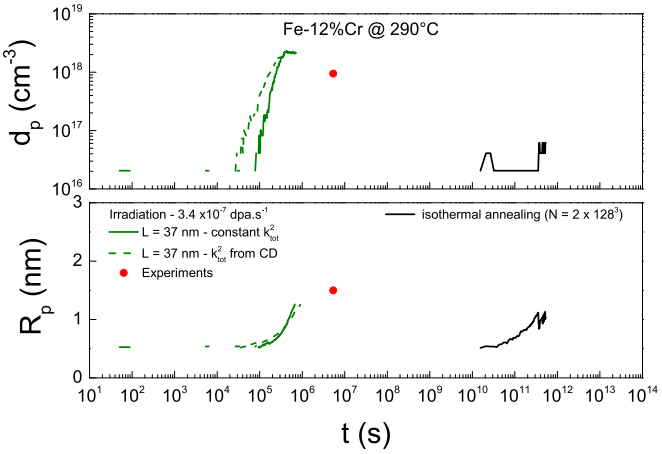

Figure 8: AKMC simulations of α–α' phase separation in Fe-12%Cr alloy during an isothermal aging at 290°C , and under irradiation at 3.4×10^{-7}dpa.s^{-1}: evolution of the density d_p and of the average radius R_p of α' precipitates.

Fe-12%Cr, 4×10^{10}s in Fe-15%Cr, and 10^{10}s in Fe-18%Cr (for the Fe-12%Cr alloy the statistics is indeed very poor, because of the small precipitate density: the simulation box contains a maximum of 5 precipitates).

When the AKMC time is rescaled to account for the CD sink strengths and point defect concentrations, there is again a good agreement with the experimental values (otherwise, the kinetics of precipitation is about 1 or 2 orders of magnitude too fast). The 12%Cr case must be considered with caution, because the simulations are too time consuming to reach the experimental dose of 1.82 dpa and because of the small system size: the experiments [18] show a homogeneous precipitation of Cr, while in the simulations (Fig. 10) precipitates only appear in the vicinity of the GB (although not on the GB itself: a PFZ of $\sim$5 nm remains around the sink). This microstructure is related to the radiation induced segregation of Cr [30]: at 290°C and for 12% of Cr, the coupling between the fluxes of point defects and the flux of Cr results in an enrichment of Cr, that can be observed of the Cr concentration profile in Fig. 11 (at 0.054 dpa for example, the composition very close to the boundary is $c_{Cr}^{GB} \sim 0.14$).

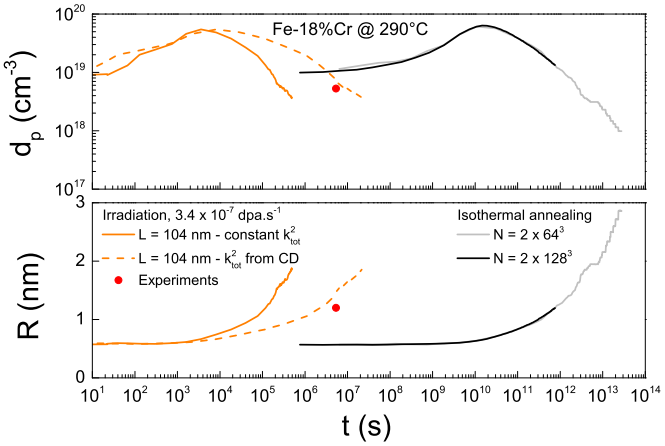

Figure 9: AKMC simulations of α–α' phase separation in Fe-18%Cr alloy during an isothermal aging at 290°C , and under irradiation at 3.4×10^{-7}dpa.s^{-1}: evolution of the density d_p and of the average radius R_p of α' precipitates.

This higher Cr concentration increases the precipitation driving force, but in the same region low point defect concentrations decrease the Cr diffusion coefficient. Precipitate nucleate and grow more rapidly in the zone where the concentration of Cr and point defects are optimum. The absence of Cr precipitates in the bulk is mainly due to the small size of the simulation: simulations of Fig. 10 have been performed with $L = 37$ nm, and at 12%Cr the nucleation rate is too small to give significant density of precipitates in such a small volume: with much larger values of L (that would unfortunately require much longer simulation times), one should observe a precipitation in the bulk, in addition to the one observed near the sinks. One can nevertheless conclude that AKMC simulations predict an acceleration of α' precipitates and a microstructure evolution in good agreement with the experiments, when the system size in large enough to observe a significant homogeneous precipitation, which is the case for Fe-15%Cr and Fe-18%Cr at 290°C.

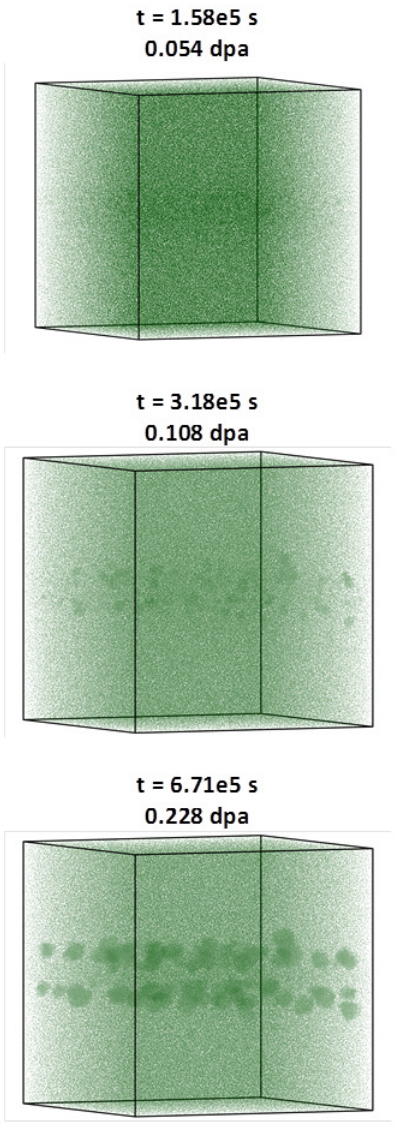

Figure 10: AKMC simulations of $\alpha - \alpha'$ phase separation in Fe-12%Cr under an irradiation at 290°C, 3.4×10^{-7}dpa.s^{-1} ($N = 2 \times 128^3$)

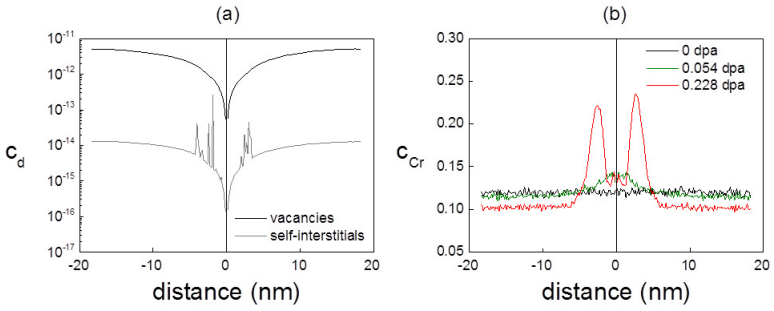

Figure 11: Point defect and Cr concentration profiles around a GB in AKMC simulations of Fe-12%Cr under irradiation at 290°C and 3.4×10^{-7}dpa.s^{-1} ($N = 2 \times 128^3$, $L = 37$ nm).

4.3. Spinodal decomposition under irradiation

AKMC simulations of isothermal annealing in Fe-32%Cr at 290°C reveal a bi-percolated $\alpha - \alpha'$ microstructure [Fig. 12(a)], as it has been observed by 3DAP at 500°C [9–11] and in previous AKMC simulations [9–11, 29]. Similar microstructures are observed in AKMC simulations under irradiation [Fig. 12(b)], except again for a PFZ near the GB. Since one can not measure the density and radius of isolated precipitates, the kinetics of precipitation is followed through the evolution of the distribution of the local Cr concentrations c_{Cr}^{loc} (defined on each site as the concentration within a sphere of radius $\sqrt{3}a \simeq 0.5$ nm, containing 59 atoms – up to the 5th nn of the site).

Fig. 13 shows the evolution of the distribution of c_{Cr}^{loc} under irradiation, with the dose rate of the experiments of Miller et al. [14]: 3.87×10^{-9}dpa.s^{-1}(we only give the kinetics with the rescaled time). It is again very similar to the one of isothermal annealing, except for an acceleration factor of $\sim 10^4$ (i.e. less than in the previous cases, due to the lower dose rate). This shows that

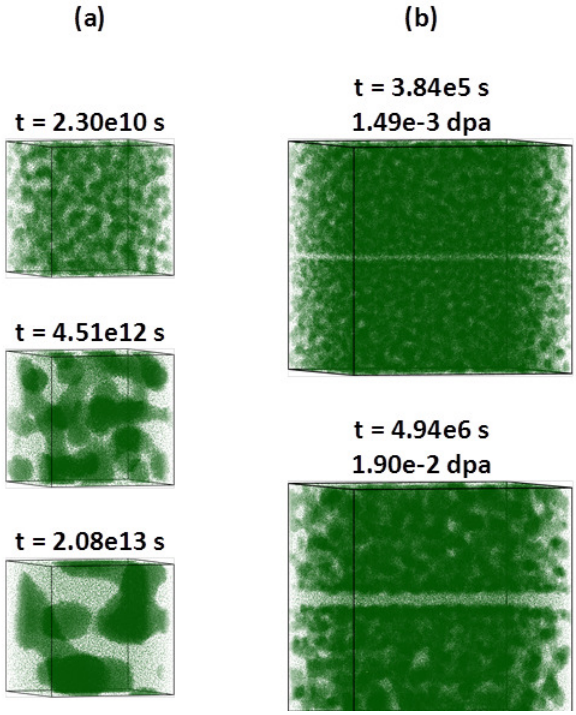

Figure 12: AKMC simulations of $\alpha - \alpha'$ phase separation in Fe-32%Cr at 290°C, (a) isothermal annealing ($N = 2 \times 64^3$), (b) irradiation at 3.87×10^{-9}dpa.s^{-1}($N = 2 \times 128^3$)

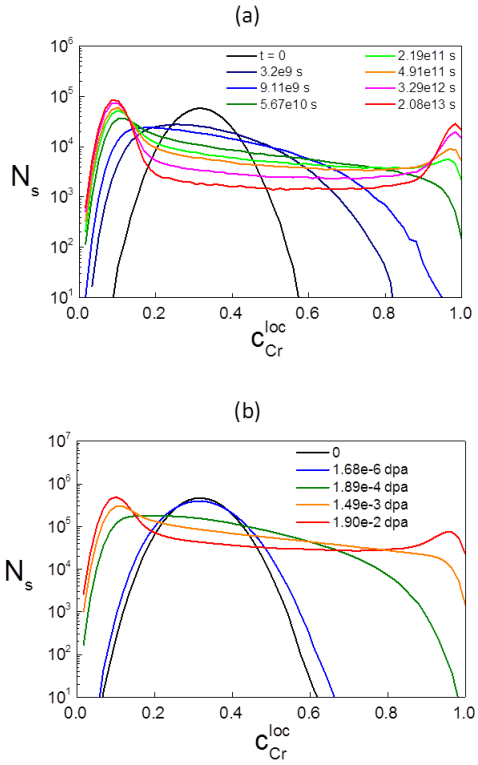

Figure 13: Evolution of the distribution of local Cr concentration in the AKMC simulation the $\alpha - \alpha'$ phase separation in Fe-32%Cr at 290°C (a) an isothermal annealing (b) under irradiation with a dose rate of 3.87×10^{-9}dpa.s^{-1} (same as in Fig. 12)

the solubility limits are not significantly affected by the irradiation at such a low flux: the concentrations at the higher dose in Fig. 13(b): $c_\alpha \simeq 0.10$ and $c_{\alpha'} \simeq 0.96$, are close to the equilibrium values (0.09 and 0.98) and will probably reach these values at longer times. The simulation seems therefore in qualitative agreement with the results of Mathon et al. [22], rather than with the conclusions drawn from Field Ion Microscopy observations by Miller and Stoller [14]. The latter were however mainly based on the observation that the precipitate volume fraction was significantly below its equilibrium value (5% instead of 25%). The dose was only of 0.03 dpa at the end of the irradiation, and fig. 13(b) suggests that the volume fraction of the α' phase is still below its final value for such a low dose. One clear difference with experiments is that isolated α' are not observed in the simulations. Further simulations and experiments at higher doses and dose rates would be useful for a better understanding of this problem of spinodal decomposition under irradiation.

4.4. Equilibrium segregation effects

The previous AKMC simulations predict that in supersaturated Fe-Cr alloys, the kinetics of $\alpha - \alpha'$ decomposition is essentially accelerated by irradiation, with no other significant change except in the vicinity of the GB. In this region, the precipitate microstructure is modified by the complex interactions between the smaller point defect concentrations and radiation-induced segregation (RIS) (see also Refs. [30, 37]). Small point defect concentrations tend to slow down Fe and Cr diffusion in the vicinity of the GB, and result in a precipitate free zone. RIS, with the parameters of our model, produces an enrichment of Cr on sinks below a threshold temperature, and a depletion above. The threshold temperature depends on the Cr concentration [30] (in Fe-10 to 15%Cr it is above 290°C: AKMC predicts a small enrichment of Cr at GB, as shown in Fig. 11). These general trends are in qualitative agreement with previous models and

some experimental results, see e.g. [38, 39], but RIS tendencies in ferritic steels are very dependent on small details of point defect migrations barriers, and therefore difficult to predict [30, 39–41].

Equilibrium segregation is another obvious phenomenon that controls the alloy composition at GBs and it may therefore modify the precipitation kinetics and precipitation microstructure. Equilibrium segregation at GBs is a complex phenomenon: the segregation energies depend on the alloy composition in the bulk and at the GB, on the GB orientation and on the details of its atomic configuration [42]. It usually produces an enrichment of Cr at GBs (see [43] and references therein) and can then reinforce or oppose to the RIS, depending on irradiation conditions. A detailed modeling of these features is beyond the scope of our study, but typical effects can be assessed. We have performed AKMC simulations including an equilibrium segregation driving force, by introducing an extra energetic term $e_{Cr}^{seg} = -0.1$ and $-0.2\,\mathrm{eV}$ when Cr atoms are located on the plane of the GB and on the two neighboring planes (e_{Cr}^{seg} is the Cr segregation energy at the GB in the dilute limit). This is the typical order of magnitude of Cr segregation energies at GBs computed with empirical potentials [44] and ab initio calculations [45].

AKMC simulations of Fe-15Cr%, under the same irradiation conditions as in the previous sections are summarized in Fig. 14 to 16. With $e_{Cr}^{seg} = -0.1\,\mathrm{eV}$, one observes a strong enrichment of Cr (up to $c_{Cr}^{GB} \simeq 0.35$) on the GB and on the two neighboring planes, but the evolution of the density and size of precipitates is the same as with $e_{Cr}^{seg} = 0$ (Fig. 15). Differences are more significant with $e_{Cr}^{seg} = -0.2\,\mathrm{eV}$: the enrichment of the two planes surrounding the sink reaches $c_{Cr}^{GB} \simeq 0.98$ (Fig. 16) and a larger depleted zone is formed around the GB (fig. 14), which is sufficient to slightly reduce the total density of precipitates and increase the average radius. This effect of the segregation is expected to

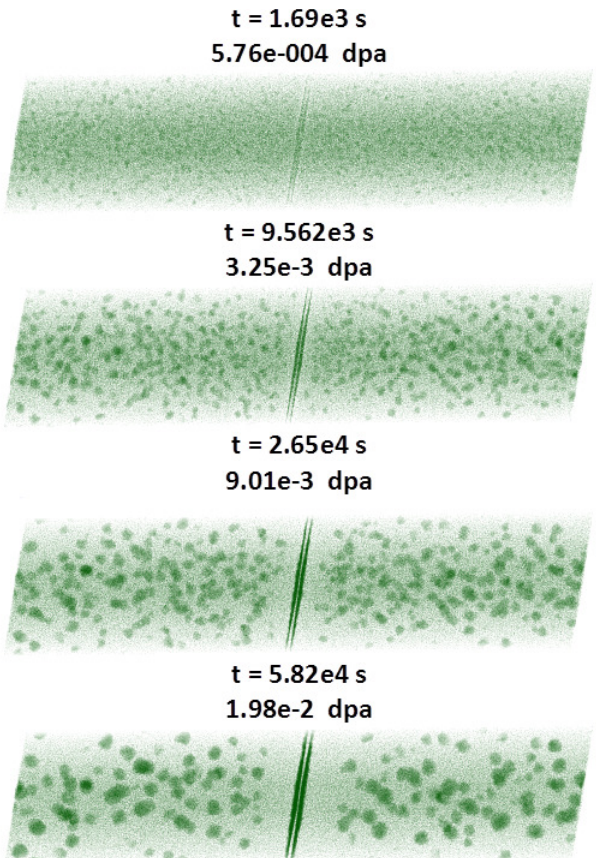

Figure 14: AKMC simulations of $\alpha - \alpha'$ phase separation in Fe-15%Cr under an irradiation at 290°C and 3.4×10^{-7}dpa.s^{-1}, with a segregation energy $e_{Cr}^{seg} = -0.2$ on the grain boundary and on the neighboring planes ($N = 64 \times 64 \times 512$)

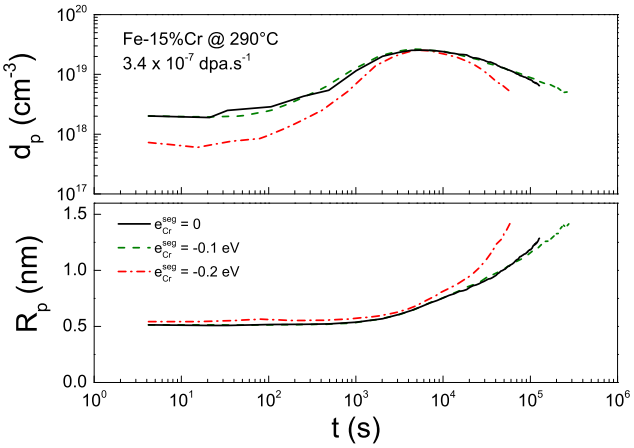

Figure 15: AKMC simulations of $\alpha - \alpha'$ phase separation in Fe-15%Cr under an irradiation at 290°C and 3.4×10^{-7}dpa.s^{-1}, with different segregation energies e_{Cr}^{seg} on the GB: evolution of the density d_p and of the average radius R_p of α' precipitates.

disappear when the distance L between sinks becomes larger (and closer to usual grain sizes), but the local modification of the precipitate distribution should persist, with also local enrichments of Cr at the GB that are much larger that the ones due to RIS.

4.5. Ballistic mixing

A striking experimental result is that α' precipitation has been observed during neutron irradiations at low dose rates (typically between 10^{-9} and 10^{-6}dpa.s^{-1} in [14, 18–21, 27]), but not under ion irradiation at higher flux (2×10^{-4}dpa.s^{-1} in [24]). One possible explanation could be the dissolution of precipitates under irradiation. This well-known phenomenon results from the chemical mixing occurring in the displacement cascades or in replacement collision sequences [46]. Ballistic mixing is dominant at high irradiation intensity (defined as $\gamma = D_{bal}/D_{th}$, the ratio of the ballistic diffusion coefficient to the thermally activated diffusion coefficient, taking into account the supersaturation of point defects), i.e. at high dose rates and low temperatures.

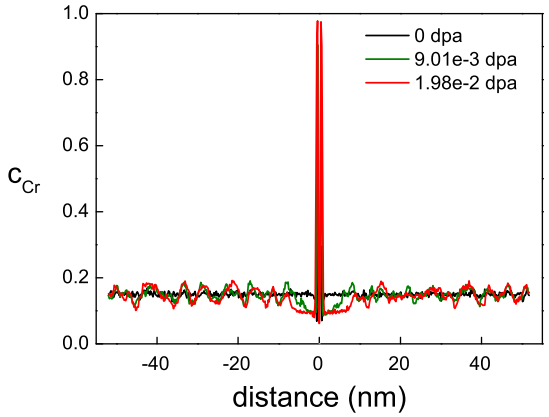

Figure 16: AKMC simulations of $\alpha - \alpha'$ phase separation in Fe-15%Cr under an irradiation at 290°C and 3.4×10^{-7}dpa.s^{-1}, with a segregation energy $e_{Cr}^{seg} = -0.2$: evolution of Cr concentration profiles.

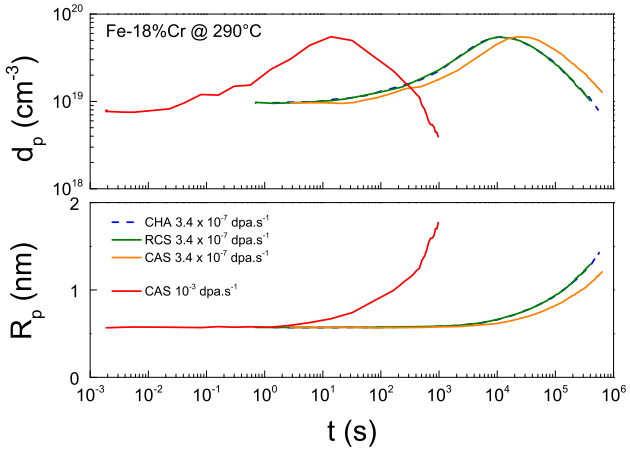

Figure 17: AKMC simulations of $\alpha - \alpha'$ phase separation in Fe-18%Cr under irradiation at 290°C, with dose rates of 3.4×10^{-7}dpa.s^{-1} and 10^{-3}dpa.s^{-1}, and point defects created by channeling (CHA), replacement collision sequences (RCS) or replacement cascades (CAS): evolution of the density d_p and of the average radius R_p of α' precipitates.

The simulation of the previous sections were performed with the simple channeling mechanism, with no replacement during the formation of the Frenkel pairs. This mechanism minimizes the ballistic mixing (although a limited one still occurs, due to the random nature of the formation and recombination of the defects). To assess the possible effects of ballistic mixing on the $\alpha-\alpha'$ precipitation, we have performed AKMC simulations with the simple mechanisms of RCS and replacement cascades described in section 3.2. Although highly idealized, they involve the main ingredient controlling the competition between the athermal mixing and the acceleration of diffusion, i.e. the number of replacements per displacement, with the correct order of magnitude (~ 10 for a RCS, ~ 100 for a displacement cascades, see e.g. [47]). AKMC simulations of α' precipitation in a Fe-18%Cr alloy under irradiation at 3.4×10^{-7}dpa.s^{-1} (with the time rescaled by Eq. (5)) are summarized in Fig. 17. One observes similar evolutions of the number and size of precipitates. The evolution with the RCS and the channeling mechanisms are indeed identical, while the simulations performed with the replacement cascades are slightly slower (by a factor ~ 2). The latter effect is simply due to lower point defects concentrations, not to ballistic mixing. The difference comes from the fact that with the channeling and RCS mechanisms, the vacancy and interstitial are created at a constant distance (10 nn), well above the recombination distance r_c (4 nn). With the replacement cascades, some pairs recombine immediately after their formation, or after a few jumps (correlated recombinations). This is indeed shown by the measurement of the point defect concentration profiles: one gets the same factor $c_v^{RCS}/c_v^{CAS} \simeq 2$. Ballistic effects are still negligible at higher flux (Fig. 17): by comparison with simulations at 3.4×10^{-7}dpa.s^{-1}, the precipitation at 10^{-3}dpa.s^{-1}(both with the replacement cascade mechanism), is simply accelerated by a factor ~ 3000 corresponding to the ratio of the dose rates. In all these cases, the irradiation

at 290°C accelerates the precipitation, but it does not dissolve the precipitates or prevent the coarsening, as predicted by simulations of model alloys at higher irradiation intensities [48].

These results are not surprising, since in the conditions of the neutron irradiations at 290°C, the irradiation intensity is low: $\gamma \sim 10^{-4}$ to 10^{-3}, depending on the sink density and the composition. Moreover, it does not change with the dose rate (the point defect elimination being dominated by sinks: $\gamma \propto G/(c_v^{st} D_v)$, with $c_v^{st} \propto G$). Ballistic mixing should however become dominant at lower T and with a low sink density, where one expects $D_{th} \propto \sqrt{G}\exp[-E_v^m/(2k_BT)]$ [31, 32] and $\gamma \propto \sqrt{G}\exp[+E_v^m/(2k_BT)]$. Unfortunately AKMC simulations become much more time consuming in such conditions, because of trapping and correlations effects (the interstitials, more especially, are strongly trapped at the $\alpha - \alpha'$ interfaces). Preliminary attempts in Fe-Cr alloys show that it is difficult to run simulations below 450K, at least with the present parameters. The development of special algorithms (see e.g. [49]) may be required to perform simulations in conditions where ballistic mixing is dominant. Experimental studies at low temperatures would be of course quite interesting, even if the slow kinetics without irradiation will prevent a direct estimation of the acceleration factor.

5. Conclusions

AKMC simulations of binary Fe-Cr alloys with 12 to 18% of Cr, show that at 290°C the $\alpha - \alpha'$ precipitation is very slow during isothermal annealing, but is strongly accelerated by irradiation, by a factor that is directly controlled by the increase of point defect concentrations.

The simulations are in good agreement with experimental studies under neutron irradiation, and predict that the acceleration is the only significant

effect on the precipitate microstructure, except in the vicinity (on a distance a few 10 nm) of the grain boundaries. In these regions, perturbations result from the interactions between the local point defect depletion, radiation-induced and equilibrium segregations. At this temperature, ballistic mixing effects are negligible, due to the rapid thermally activated diffusion of point defects in iron alloys. This suggests that the lack of precipitation observed during ion irradiation at high dose rates is not due to the ballistic dissolution of precipitates.

These conclusions are drawn from a simple model of binary Fe-Cr alloys. The materials used in experimental studies always contains other minor alloying elements and impurities. Some of them have very strong interactions with point defects (the interactions between direct interstitials C, N, O with vacancies are especially attractive [50]). The fact that our model is in good agreement with the experiments suggests that they do not significantly affect the kinetics of α' precipitation under irradiation. But they could affect the distribution of point defect clusters: recent SANS studies have revealed, in addition to α' precipitates, the formation of small Cr-C clusters under neutron irradiation [51]. Co-segregations of Cr and C at GBs have been also observed under irradiation [43]. It is hoped that the integration of carbon in the AKMC simulations will provide further insights into such observations. The modeling of GBs could also be improved (e.g. with a detailed fitting of the segregation energies or by taking into account the local acceleration of diffusion). However, the radiation accelerated precipitation in Fe-Cr appears to be less sensitive to the details of point defect properties, and therefore more predictible than RIS, using simple diffusion models as those used in the present study.

Acknowledgments

We thank Enrique Martinez, Orianne Senninger, Estelle Meslin and Alain Barbu for useful discussions. This research has received partial funding from Eurofusion IReMEV programme and from the European Atomic Energy Community's (Euratom) Seventh Framework Programme FP7/2007-2013 under grant agreement No. 604862 (MatISSE project), in the framework of the EERA (European Energy Research Alliance) Joint Programme on Nuclear Materials.

References

[1] R. Fisher, E. Dulis, K. Carroll, Identification of the precipitate accompanying 885 f embrittlement in chromium steels, Trans. AIME 197 (1953) 690–695.

[2] G. Bonny, D. Terentyev, L. Malerba, New contribution to the thermodynamics of fe-cr alloys as base for ferritic steels, J. Phase Equilib. Diff. 31 (2010) 439–444.

[3] M. Furusaka, Y. Ishikawa, S. Yamaguchi, Y. Fujino, Phase separation process in fecr alloys studied by neutron small angle scattering, J. Phys. Soc. Jpn. 55 (1986) 2253–2269.

[4] F. Bley, Neutron small-angle scattering study of unmixing in Fe–Cr alloys, Acta Metall. Mater. 40 (1992) 1505 – 1517.

[5] T. de Nys, P. Gielen, Spinodal decomposition in the fe-cr system, Metall. Trans. 2 (1971) 1423–1428.

[6] S. M. Dubiel, J. Cieslak, Short-range order in iron-rich fe-cr alloys as revealed by mössbauer spectroscopy, Phys. Rev. B 83 (2011) 180202.

[7] S. Dubiel, J. Zukrowski, Change of cr atoms distribution in Fe85-Cr15 alloy caused by 250 kev he+ ion irradiation to different doses, J. Alloys Compd. 624 (2015) 165 – 169.

[8] S. Brenner, M. Miller, W. Soffa, Spinodal decomposition of iron-32 at.% chromium at 470°C), Scripta Metall. 16 (1982) 831 – 836.

[9] M. Miller, J. Hyde, M. Hetherington, A. Cerezo, G. Smith, C. Elliott, Spinodal decomposition in fe-cr alloys: Experimental study at the atomic level and comparison with computer models – i. introduction and methodology, Acta Metall. Mater. 43 (1995) 3385 – 3401.

[10] J. Hyde, M. Miller, M. Hetherington, A. Cerezo, G. Smith, C. Elliott, Spinodal decomposition in fe-cr alloys: Experimental study at the atomic level and comparison with computer models – ii. development of domain size and composition amplitude, Acta Metall. Mater. 43 (1995) 3403 – 3413.

[11] J. Hyde, M. Miller, M. Hetherington, A. Cerezo, G. Smith, C. Elliott, Spinodal decomposition in fe-cr alloys: Experimental study at the atomic level and comparison with computer models – iii. development of morphology, Acta Metall. Mater. 43 (1995) 3415 – 3426.

[12] F. Danoix, P. Auger, Atom probe studies of the fe-cr system and stainless steels aged at intermediate temperature: A review, Mater. Charact. 44 (2000) 177 – 201.

[13] S. Novy, P. Pareige, C. Pareige, Atomic scale analysis and phase separation understanding in a thermally aged fe-20 at.%cr alloy, J. Nucl. Mater. 384 (2009) 96 – 102.

[14] M. Miller, R. Stoller, K. Russell, Effect of neutron-irradiation on the spinodal decomposition of fe-32% cr model alloy, J. Nucl. Mater. 230 (1996) 219 – 225.

[15] W. Xiong, M. Selleby, Q. Chen, J. Odqvist, Y. Du, Phase equilibria and thermodynamic properties in the fe-cr system, Crit. Rev. Solid State 35 (2010) 125–152.

[16] R. Klueh, A. Nelson, Ferritic/martensitic steels for next-generation reactors, J. Nucl. Mater. 371 (2007) 37 – 52.

[17] J.-L. Boutard, V. Badjeck, L. Barguet, C. Barouh, A. Bhattacharya, Y. Colignon, C. Hatzoglou, M. Loyer-Prost, A. Rouffié, N. Sallez, H. Salmon-Legagneur, T. Schuler, Oxide dispersion strengthened ferritic steels: a basic research joint program in france, J. Nucl. Mater. 455 (2014) 605 – 611.

[18] M. Bachhav, G. R. Odette, E. A. Marquis, α' precipitation in neutron-irradiated fe-cr alloys, Scripta Mater. 74 (2014) 48 – 51.

[19] V. Kuksenko, C. Pareige, P. Pareige, Intra granular precipitation and grain boundary segregation under neutron irradiation in a low purity fe-cr based alloy, J. Nucl. Mater. 425 (2012) 125 – 129.

[20] V. Kuksenko, C. Pareige, P. Pareige, Cr precipitation in neutron irradiated industrial purity fe-cr model alloys, J. of Nucl. Mater. 432 (2013) 160 – 165.

[21] F. Bergner, A. Ulbricht, C. Heintze, Estimation of the solubility limit of cr in fe at 300°C from small-angle neutron scattering in neutron-irradiated fe-cr alloys, Scripta Mater. 61 (2009) 1060 – 1063.

[22] M. Mathon, Y. de Carlan, G. Geoffroy, X. Averty, A. Alamo, C. de Novion, A sans investigation of the irradiation-enhanced $\alpha - \alpha'$ phases separation in 7-12 cr martensitic steels, J. Nucl. Mater. 312 (2003) 236 – 248.

[23] W.-Y. Chen, Y. Miao, Y. Wu, C. A. Tomchik, K. Mo, J. Gan, M. A. Okuniewski, S. A. Maloy, J. F. Stubbins, Atom probe study of irradiation-enhanced α' precipitation in neutron-irradiated fe–cr model alloys, J. Nucl. Mater. 462 (2015) 242 – 249.

[24] C. Pareige, V. Kuksenko, P. Pareige, Behaviour of p, si, ni impurities and cr in self ion irradiated fe-cr alloys: Comparison to neutron irradiation, J. Nucl. Mater. 456 (2015) 471 – 476.

[25] A. R. Gokhman, A. Ulbricht, U. Birkenheuer, F. Bergner, Cluster dynamics study of neutron irradiation induced defects in fe-12.5at%cr alloy, Solid State Phenom. 172-174 (2011) 449–457.

[26] E. Little, D. Stow, Void-swelling in irons and ferritic steels: Ii. an experimental survey of materials irradiated in a fast reactor, J. Nucl. Mater. 87 (1979) 25 – 39.

[27] M. Bachhav, G. R. Odette, E. A. Marquis, Microstructural changes in a neutron-irradiated fe-15at.%cr alloy, J. Nucl. Mater. 454 (2014) 381 – 386.

[28] E. Martínez, O. Senninger, C.-C. Fu, F. Soisson, Decomposition kinetics of fe-cr solid solutions during thermal aging, Phys. Rev. B 86 (2012) 224109.

[29] O. Senninger, E. Martínez, F. Soisson, M. Nastar, Y. Bréchet, Atomistic simulations of the decomposition kinetics in fe-cr alloys, Acta Mater. 73 (2014) 97 – 106.

[30] O. Senninger, F. Soisson, E. Martínez, M. Nastar, C. Fu, Y. Bréchet, Mod-

eling radiation induced segregation in fe-cr alloys, Acta Mater. 103 (2016) 1 – 11.

[31] R. Sizmann, The effect of radiation upon diffusion in metals, J. Nucl. Mater. 6970 (1978) 386 – 412.

[32] G. S. Was, Fundamentals of Radiation Materials Science, Springer-Verlag, 2007.

[33] F. Nichols, On the estimation of sink-absorption terms in reaction-rate-theory analysis of radiation damage, J. Nucl. Mater. 75 (1978) 32 – 41.

[34] T. Jourdan, G. Bencteux, G. Adjanor, Efficient simulation of kinetics of radiation induced defects: A cluster dynamics approach, J. Nucl. Mater. 444 (2014) 298 – 313.

[35] E. Meslin, A. Barbu, L. Boulanger, B. Radiguet, P. Pareige, K. Arakawa, C. Fu, Cluster-dynamics modelling of defects in α-iron under cascade damage conditions, J. Nucl. Mater. 382 (2008) 190 – 196.

[36] M. Nastar, F. Soisson, Atomistic modeling of phase transformations: Point-defect concentrations and the time-scale problem, Phys. Rev. B 86 (2012) 220102.

[37] F. Soisson, Kinetic monte carlo simulations of radiation induced segregation and precipitation, J. Nucl. Mater. 349 (2006) 235 – 250.

[38] J. P. Wharry, Z. Jiao, G. S. Was, Application of the inverse kirkendall model of radiation-induced segregation to ferritic martensitic alloys, J. Nucl. Mater. 425 (2012) 117 – 124.

[39] J. P. Wharry, G. S. Was, The mechanism of radiation induced segregation in ferritic martensitic alloys, Acta Mater. 65 (2014) 42 – 55.

[40] S. Choudhury, L. Barnard, J. Tucker, T. Allen, B. Wirth, M. Asta, D. Morgan, Ab-initio based modeling of diffusion in dilute bcc fe-ni and fe-cr alloys and implications for radiation induced segregation, J. Nucl. Mater. 411 (2011) 1 – 14.

[41] L. Messina, M. Nastar, T. Garnier, C. Domain, P. Olsson, Exact *ab initio* transport coefficients in bcc Fe $-$ x (x = Cr, Cu, Mn, Ni, P, Si) dilute alloys, Phys. Rev. B 90 (2014) 104203.

[42] L. Priester, Grain Boundaries, Springer Netherlands, 2013.

[43] E. A. Marquis, R. Hu, T. Rousseau, A systematic approach for the study of radiation-induced segregation/depletion at grain boundaries in steels, J. Nucl. Mater. 413 (2011) 1 – 4.

[44] D. Terentyev, X. He, E. Zhurkin, A. Bakaev, Segregation of cr at tilt grain boundaries in fe-cr alloys: A metropolis monte carlo study, J. Nucl. Mater. 408 (2011) 161 – 170.

[45] C.-C. Fu, private communication.

[46] G. Martin, P. Bellon, Driven alloys, in: H. Ehrenreich, F. Spaepen (Eds.), Advances in Research and Applications, volume 50 of *Solid State Physics*, Academic Press, 1996, pp. 189 – 331.

[47] C. Becquart, C. Domain, A. Legris, J. V. Duysen, Influence of the interatomic potentials on molecular dynamics simulations of displacement cascades, J. Nucl. Mater. 280 (2000) 73 – 85.

[48] R. A. Enrique, P. Bellon, Compositional patterning in immiscible alloys driven by irradiation, Phys. Rev. B 63 (2001) 134111.

[49] M. Athènes, V. V. Bulatov, Path factorization approach to stochastic simulations, Phys. Rev. Lett. 113 (2014) 230601.

[50] C. Barouh, T. Schuler, C.-C. Fu, M. Nastar, Interaction between vacancies and interstitial solutes (c, n, and o) in α-fe: From electronic structure to thermodynamics, Phys. Rev. B 90 (2014) 054112.

[51] C. Heintze, F. Bergner, A. Ulbricht, H. Eckerlebe, The microstructure of neutron-irradiated fe-cr alloys: A small-angle neutron scattering study, J. Nucl. Mater. 409 (2011) 106 – 111.